Radboud Repository

Radboud University Nijmegen

PDF hosted at the Radboud Repository of the Radboud University Nijmegen

A BROADBAND RADIO STUDY OF THE AVERAGE PROFILE AND GIANT PULSES FROM PSR B1821−24A

A. V. Bilous[1,2], T. T. Pennucci[2], P. Demorest[3], and S. M. Ransom[4]
version 3.2

ABSTRACT

We present the results of a wideband (720−2400 MHz) study of PSR B1821−24A (J1824−2452A, M28A), an energetic millisecond pulsar visible in radio, X-rays and γ-rays. In radio, the pulsar has a complex average profile which spans $\gtrsim 85\%$ of the spin period and exhibits strong evolution with observing frequency. For the first time we measure phase-resolved polarization properties and spectral indices of radio emission throughout almost all of the on-pulse window. We synthesize our findings with high-energy information to compare M28A to other known γ-ray millisecond pulsars and to speculate that M28A's radio emission originates in multiple regions within its magnetosphere (i.e. both in the slot or outer gaps near the light cylinder and at lower altitudes above the polar cap). M28A is one of the handful of pulsars which are known to emit Giant Pulses (GPs) – short, bright radio pulses of unknown nature. We report a drop in the linear polarization of the average profile in both windows of GP generation and also a 'W'-shaped absorption feature (resembling a double notch), partly overlapping with one of the GP windows. The GPs themselves have broadband spectra consisting of multiple patches with $\Delta\nu/\nu \sim 0.07$. Although our time resolution was not sufficient to resolve the GP structure on the μs scale, we argue that GPs from this pulsar most closely resemble the GPs from the main pulse of the Crab pulsar, which consist of a series of narrowband nanoshots.

Keywords: stars − pulsars: individual (B1821-24A)

1. INTRODUCTION

PSR B1821−24A (hereafter M28A) is an isolated 3.05-millisecond pulsar (MSP) in the globular cluster Messier 28 (Lyne et al. 1987). The pulsar has an uncommonly large period derivative, $\dot{P} = 1.62 \times 10^{-18}$ s s^{-1} (Foster et al. 1988; Verbiest et al. 2009), about two orders of magnitude larger than typical $\dot{P}$ values for MSPs. The large observed $\dot{P}$ is a reasonable estimate of the pulsar's magnetic braking: based on the measured proper motion of the pulsar and the models of the gravitational potential inside the cluster, Johnson et al. (2013, hereafter J13) showed that no more than 14% of the observed $\dot{P}$ can be caused by the accelerated motion in the cluster's gravitational potential and the Shklovskii effect.

M28A is, in many regards, an extreme member of the MSP population. It is the most energetic MSP known, with an inferred spin-down luminosity ($\dot{E} \propto P^{-3}\dot{P}$) of 2.2×10^{36} erg s^{-1}. M28A has the second-to-largest (after B1937+21) inferred value of the strength of the magnetic field evaluated at the light cylinder ($B_{\rm LC} \propto P^{-2.5}\dot{P}^{0.5}$, 7.2×10^5 G). The pulsar has known irregularities in its spin-down (timing noise; J13, Verbiest et al. 2009) and was reported to have a microglitch (Cognard & Backer 2004).

Pulsed emission from M28A had been detected in radio (Lyne et al. 1987), X-ray (Saito et al. 1997) and γ-rays

(Wu et al. 2013, J13). So far, combining the information from different parts of the electromagnetic spectrum has proven to be inconclusive and suggested a complex relationship between the emission regions (J13).

In radio, M28A has a complex multi-peaked profile, which spans almost the whole pulsar spin period. The profile has a high degree of linear polarization and exhibits strong evolution as a function of frequency (Ord et al. 2004). Unlike the majority of X-ray-detected MSPs, which show broad thermal X-ray pulsations, M28A's X-ray profile consists of two sharp peaks of highly beamed, non-thermal magnetospheric radiation (Zavlin 2007; Bogdanov et al. 2011). In γ-rays the pulsar has two broad peaks which are roughly coincident with two out of the three main radio peaks. It is hard to classify M28A as a Class I, II or III γ-ray pulsar (with classes defined by the relative phase lag between the radio/γ-ray profile peaks and presumably different radio/γ-ray emission regions; see Johnson et al. 2014), although no direct simulation of γ-ray light curves had been performed so far (J13).

Similar to other pulsars with magnetospheric X-ray emission and comparable values of $B_{\rm LC}$ and $\dot{E}$, M28A is known to emit giant radio pulses (GPs; Romani & Johnston 2001). GPs are a rare (known only for a handful of pulsars) type of single pulses of unknown origin. GPs are usually distinguished by their large brightness temperature (up to 5×10^{39} K), short duration (ns – μs) and power-law energy distribution (see Knight 2006, and references therein).

In this work we analyze an extensive set of broadband, (720−920, 1100−1900, and 1700−2400 MHz) full-Stokes observations of M28A. The high signal-to-noise ratio (S/N) of the accumulated average profiles, together with the large fractional bandwidth, allowed us to measure the phase-resolved spectral and polarization prop-

[1] Department of Astrophysics/IMAPP, Radboud University Nijmegen, P.O. Box 9010, 6500 GL Nijmegen, the Netherlands a.bilous@science.ru.nl
[2] Department of Astronomy, University of Virginia, PO Box 400325, Charlottesville, VA 22904, USA
[3] National Radio Astronomy Observatory, P.O. Box O, Socorro, NM 87801, USA
[4] National Radio Astronomy Observatory, 520 Edgemont Road, Charlottesville, VA 22903, USA

erties even of the faint profile components, thus substantially improving upon similar such measurements previously made by Foster (1990) and Yan et al. (2011b). Such measurements will facilitate constraining the location of the radio emission regions and will help multiwavelength light curve modeling (Guillemot et al. 2012). We also collected the largest-to-date sample of M28A's GPs, which is an order of magnitude larger than the sample used in the most recent previous study (Knight et al. 2006a, hereafter K06a). For the first time we were able to explore broadband spectra of M28A's GPs and compare them to similar studies of GPs from B1937+21 and the Crab pulsar. This is interesting because it is still unclear which properties are common to all GPs, and whether GPs have more than one emission mechanism (Hankins & Eilek 2007).

The rest of the paper is organized as follows. After describing the calibration and correction for propagation effects (Section 2), we describe the properties of the average profile (Section 3) and the giant pulses (Section 4), comparing the latter to the GPs from the Crab pulsar and PSR B1937+21. In Section 5 we compare the properties of M28A to the MSPs from the second Fermi catalog (Abdo et al. 2013) and speculate on the location of the radio emission regions in the magnetosphere of M28A. A short summary is given in Section 6.

2. INITIAL DATA PROCESSING

M28A was observed with the 100 m Robert C. Byrd Green Bank Telescope during 21 sessions in $2010-2013$. The signal was recorded with the GUPPI[5] pulsar backend in the coherent dedisperion search mode (DuPlain et al. 2008). In this mode, raw voltages were sampled with a time resolution of 1/BW (where BW is the bandwidth). Each 512-sample block was Fourier transformed and the signal was coherently dedispersed within each frequency channel using the average dispersion measure (DM) for the pulsars in the globular cluster M28[6], $120\,\mathrm{pc\,cm^{-3}}$. After square-law detection, several consecutive Fourier spectra were averaged together to meet the disk write speed limits.

Table 1 summarizes some details of the observations. Following the standard IEEE (Institute of Electrical and Electronics Engineers) radio frequency naming convention[7], the observations with the central frequencies of $820\,\mathrm{MHz}$, $1500\,\mathrm{MHz}$ and $2000\,\mathrm{MHz}$ will be hereafter referred to as UHF, L-band and S-band observations. In all three bands the time resolution of single-pulse data was $t_{\mathrm{res}} = 10.24\,\mu\mathrm{s}$ and the number of bins in the folded profiles $n_{\mathrm{bin}} = 298$ was chosen to match t_{res} closely. However, the UHF single-pulse data were rewritten with four times lower time/frequency resolution shortly after making folded pulse profiles, and so only these data with $t_{\mathrm{res}} = 40.96\,\mu\mathrm{s}$ and a frequency resolution of $1.56\,\mathrm{MHz}$ were available for the UHF part of our GP analysis.

All further data reduction was done using the PSRCHIVE[8] and PRESTO[9] software packages (Hotan et al. 2004; van Straten et al. 2012; Ransom

[5] https://safe.nrao.edu/wiki/bin/view/CICADA/NGNPP
[6] http://www.naic.edu/$\sim$pfreire/GCpsr.html
[7] http://standards.ieee.org/findstds/standard/521-2002.html
[8] http://psrchive.sourceforge.net/
[9] http://www.cv.nrao.edu/∼sransom/presto/

Table 1
Observing summary. The columns are: name of the band, its central frequency, bandwidth, number of channels, time resolution, number of observing sessions per band and the total observing time.

Band name	ν_c (MHz)	BW (MHz)	N_{chan}	t_{res} (μs)	N_{sess}	Total time (hr)
UHF	820	200	512[a]	10.24[a]	1	2.6
L	1500	800[b]	512	10.24	11	27.1
S	2000	800[b]	512	10.24	9	14.6

[a]For the GP analysis, only the data with $t_{\mathrm{res}} = 40.96\,\mu\mathrm{s}$ and $N_{\mathrm{chan}} = 128$ were available.
[b]Some fraction of the band was affected by terrestrial radio frequency interference, see text for details.

2001).

The observations presented in this work were a part of the larger dataset analyzed in Pennucci et al. (2014, hereafter PDR14) and we folded our data with the ephemeris determined from PDR14's dataset. The root-mean-square (RMS) deviation of timing residuals, obtained from this ephemeris was $1.35\,\mu\mathrm{s}$, much smaller than the time resolution of our data.

Prior to each observation we recorded a pulsed calibration signal, which was used together with standard unpolarized flux calibrators (quasars B1442+101 for L-band and 3C190 for S-band and the UHF observations) to correct for the instrumental response of the receiver system. Polarization calibration for L-band and the UHF observations was conducted using predetermined Mueller matrix solutions, which described the cross-coupling between orthogonal polarizations in the receivers (van Straten 2004). The Mueller matrix was determined using the PSRCHIVE task `pcm` based on observations of PSR B0450+55 in L-band and PSR B1744−21A in the UHF band. For S-band polarization calibration we assumed that the feed is ideal and composed of two orthogonally polarized receptors. The equivalent flux of the local pulsed calibration signal was determined separately in each polarization using observations of the unpolarized source 3C190. The calibration signal measurements were used to balance the gain of each polarization in our S-band observations of M28A. Comparing the polarization of the average profile in the frequency region where L- and S-band overlap did not reveal any significant discrepancies between the L- and S-band polarization data. In this work we use the standard PSRCHIVE PSR/IEEE convention for the sign of circular polarization, described in van Straten et al. (2010).

The data in approximately 5% of the frequency channels in the UHF band, 25% of channels in L-band and 20% in S-band were affected by radio frequency interference (RFI) and removed during the calibration (see Fig. 1 in PDR14).

2.1. Selection of GP candidates

The search for GP candidates was done in the following manner. First, we used PRESTO to dedisperse and band-integrate the raw data with the DM from Section 2.2. When necessary, we applied an RFI mask, calculated from a small subset of data for each session. This

resulted in one-dimensional, uncalibrated total intensity time series. Then, the candidates were selected from these time series using `single_pulse_search.py` from PRESTO. This routine a) normalizes a chunk of data (setting its mean to 0 and RMS to 1); b) convolves the data with a series of boxcar functions of varying width n and a height of $1/\sqrt{n}$; c) selects the candidates from the convolved signal that have peak values above a user-specified threshold; d) sifts the duplicate candidates (i.e. those candidates that are above the threshold for different boxcar widths, but have the same time of arrival) by comparing the convolved signals corresponding to different boxcar widths and selecting the width that gives the largest peak value in the convolved signal. Such an optimal width n_{opt} will be close to the observed pulse width as seen in the original time-series.

We set the lower limit on the boxcar width to one sample and the upper limit to six samples. The upper limit corresponds to the candidate width of $61\,\mu$s for L- and S-band and $246\,\mu$s for the UHF band, which is much larger than the expected width of GPs according to K06a. The selection threshold was set to $\mathrm{SN_{thr}} = 7$.

Note that since candidate selection is performed on the convolved signal, this results in an effective width-dependent S/N threshold of $7/\sqrt{n_{\mathrm{opt}}}$ for the signal with original time resolution. The averaging of the signal over n_{opt} samples in the convolution reduces the noise variance by the same factor, introducing the $1/\sqrt{n_{\mathrm{opt}}}$ dependence in the S/N threshold (see details in Bilous et al. 2012).

Knowing the time of arrival of each event, we dedispersed, calibrated and removed the Faraday rotation for the corresponding portions of raw data in the same way as for the average profile. About 4% of candidates were discarded since no pulses were revealed during a visual inspection of both the band-averaged and frequency-resolved calibrated data. Such candidates were most likely due to short intermittent RFI (missed by a constant RFI mask, but removed during calibration).

Note that since some RFI showed intermittency on short (about a minute) timescales, the number of corrupted channels varied from one GP to another and did not necessarily coincide with the number of channels removed from the time-averaged data from the same observing session.

2.2. Correction for dispersion from the interstellar medium (ISM)

PDR14 measured the dispersion measure for each of their observing sessions by fitting a two-dimensional (frequency/phase) model of the pulse profile to the time-averaged data from each session. Such method allows one to measure the variation of DM between the sessions quite precisely (e.g. $6 \times 10^{-5}\,\mathrm{pc\,cm^{-3}}$ for our L-band sessions in PDR14), but it leaves the absolute value of DM unknown to within some constant value that depends on the choice of profile model. Microsecond-long, bright and broadband GPs offer a cross-check on DM determination (K06a). For our observing setup, however, the precision of $\mathrm{DM_{GP}}$ obtained by maximizing S/N of a giant pulse over the set of trial DMs was limited by the coarse time resolution, which exceeded the expected width of GP. In this case, the uncertainty in

$\mathrm{DM_{GP}}$ approximately corresponds to the amount of DM variation, needed to cause the signal delay of t_{res} between the top and the bottom of the band. This expected DM uncertainty matched well the standard deviation of the $\mathrm{DM_{GP}}$ values within a single observing session (typically, $0.002\,\mathrm{pc\,cm^{-3}}$ for L-band, $0.006\,\mathrm{pc\,cm^{-3}}$ for S- and the UHF bands, two orders of magnitude larger than in PDR14). Nevertheless, in all three bands, in each observing session the values of $\mathrm{DM_{GP}}$ were significantly larger than the corresponding $\mathrm{DM_{PDR14}}$ for that session and, when dedispersed with $\mathrm{DM_{PDR14}}$, GPs showed visible dispersive delay at the lower edge of the band. The low number of pulses per session (especially in S-band, where some sessions had less than 5 GPs) limited the possibility of refining DM measurements by averaging DMs from individual GPs. Thus, for the subsequent analysis we chose not to use $\mathrm{DM_{GP}}$ directly, but rather dedispersed the data with $\mathrm{DM_{fold}} = \mathrm{DM_{PDR14}}(t) + const$, where $const = 0.011\,\mathrm{pc\,cm^{-3}}$ was the average difference between $\mathrm{DM_{GP}}$ and $\mathrm{DM_{PDR14}}$ for all sessions.

Phase-resolved measurements of position angle or spectral index in Section 3 are somewhat sensitive (especially near the edges of profile components) to the value of DM used for folding. To probe the influence of the uncertainty in $\mathrm{DM_{fold}}$ on the phase-resolved measurements, we repeated the analysis described in Section 3 for the data folded with $\mathrm{DM_{fold}} \pm 0.005\,\mathrm{pc\,cm^{-3}}$. Such an estimate of uncertainty in $\mathrm{DM_{fold}}$ corresponded to the typical standard deviation of $\mathrm{DM_{GP}}$ within a single session, averaged between the three observing bands. The discrepancies between the values of phase-resolved parameters obtained for different $\mathrm{DM_{fold}}$ were further incorporated into the measurement uncertainties (see Fig. 1(d−f)).

2.3. Correction for Faraday rotation

The propagation of a linearly polarized wave through the magnetized plasma in the interstellar medium causes the wave's position angle (PA) to rotate by an angle proportional to the square of its wavelength. The coefficient of the proportionality, called the rotation measure (RM), was estimated for each session by fitting the function $\mathrm{PA} = \mathrm{RM} \times (c/\nu)^2 + const$ to the position angle of emission in the two phase windows containing the brightest and most polarized profile components (P1 and P2, following the convention in Backer & Sallmen 1997, also see Fig. 1(a)). The measured values of RM were a sum of interstellar $\mathrm{RM_{IS}}$ and a contribution from Earth's ionosphere $\mathrm{RM_{iono}}$, with the latter depending on the total electron content along the line of sight and the orientation of the line of sight with respect to the Earth's magnetic field. We estimated $\mathrm{RM_{iono}}$ with the `ionFR`[10] software (Sotomayor-Beltran et al. 2013), which uses the International Geomagnetic Reference Field (IGRF11) and global ionospheric maps to predict $\mathrm{RM_{iono}}$ along a given line of sight at a specific geographic location. For our set of parameters, $\mathrm{RM_{iono}}$ varied from 1 to 6 rad m^{-2}, and changed by $0.2-1.5$ rad m^{-2} during an observing session.

The typical uncertainty of a single-epoch measurement of $\mathrm{RM_{IS}} = \mathrm{RM} - \mathrm{RM_{iono}}$ was about 1 rad m^{-2}. The values of $\mathrm{RM_{IS}}$ from 21 observing sessions did not show

---

[10] http://sourceforge.net/projects/ionfr/

any apparent secular variation with time, being randomly scattered around an average value of 82.5 rad m^{-2} with an RMS of 2.1 rad m^{-2}. The most recent value for RM$_{IS}$ = 77.8 ± 0.6 rad m^{-2}, obtained by Yan et al. (2011a), is somewhat lower, but still in agreement with our measurement.

2.4. *Scintillation and scattering*

The giant pulses that we detected in the UHF band and in some of the L-band sessions displayed a typical fast-rise/exponential-decay shape. This is indicative of the GPs having traversed an inhomogeneous ISM (Fig. 4), and it allowed us to estimate the scattering time τ_{sc} for these sessions. For each session, we constructed an average GP by summing the GPs aligned by the phase of half-maximum intensity on the rising edge and then fit one-sided exponential to the trailing side of the average GP. In our single UHF epoch, $\tau_{sc} = 100 \pm 40\,\mu$s. In L-band, τ_{sc} varied between sessions, from being virtually undetectable even at the lower edge of the band, $\tau_{sc}(1174.5\,\text{MHz}) < 10\,\mu$s, to being as large as $\tau_{sc}(1174.5\,\text{MHz}) = 25 \pm 8\,\mu$s. The sessions which were separated by about a month or less usually had similar scattering time. The variability of τ_{sc} was previously noted by K06a and our measurements are consistent with τ_{sc} of 24.5 μs measured at 1 GHz by Foster (1990).

If $\tau_{sc}(1200\,\text{MHz}) \approx 15\,\mu$s and the spectrum of turbulence is Kolmogorov, then the decorrelation bandwidth $\delta f \approx 1/(2\pi\tau_{sc})$ ranges from 1 kHz at 720 MHz to 220 kHz at 2400 MHz, which is much smaller than our frequency resolution at all observing frequencies (390 kHz in the UHF band and 1.56 MHz in L- and S-band). Since many scintles are averaged within one frequency channel, we do not see any signs of diffractive scintillation in the observed spectrum of M28A's emission. However, we record the variation of the pulsar's flux between observing sessions. The modulation index of such variation ($m = \sigma_I/\langle I \rangle$, where σ_I is the standard deviation of the observed flux densities and $\langle I \rangle$ is their mean) was 0.11 for the eleven L-band observations and 0.17 for the nine S-band sessions. It is interesting to compare the observed flux modulation with the prediction for refractive scintillation (RISS). The predicted characteristic timescale of refractive scintillation changes from 50 days at 1100 MHz to 10 days at 2400 MHz, assuming the pulsar's transverse velocity to be 200 km s^{-1} (J13). The expected modulation index for RISS is given by the decorrelation bandwidth of diffractive scintillation at a given frequency, $m_{RISS} = (\delta f/f)^{1/6}$ (Rickett 1996). For the center frequencies of L- and S-bands, m_{RISS} is expected to be equal to 0.19 and 0.22 respectively, roughly consistent with the observed flux modulation.

3. AVERAGE PROFILE

Fig. 1(a) shows M28A's average profile, obtained by accumulating the signal from 27 hours of observations at L-band. The peak of the brightest component at 1500 MHz was aligned to phase 0.5, and the components near phases 0.2, 0.5 and 0.7 are labeled P1/P2/P3, following the convention of Backer & Sallmen (1997). Additionally, we used "P0" to label the faint precursor to component P1 (this precursor also appears in profiles presented by Yan et al. (2011b) and J13). For the complete, frequency-resolved representation of M28A's total

intensity profiles between 720 and 2400 MHz we refer the reader to Fig. 1 in PDR14.

One of the early works on M28A suggested that this pulsar may have two distinct emission modes. According to Backer & Sallmen (1997), the peak intensity of P2 was three times smaller than the peak intensity of P1 for one third of their observing time at 1395 MHz (so-called "abnormal mode"). For the rest of the time P2 was about two times brighter than P1 ("normal mode"). At the same time, the peak ratio at 800 MHz did not show any temporal variations down to 25% accuracy. Romani & Johnston (2001) reported that in their observations at 1518 MHz, P2's relative flux (with respect to P1 and P3) decreased by 25% during the first hour of observations and stabilized after that. Our data do not show any signs of such behavior. The peak intensity ratio P2/P1, estimated by averaging 5 minutes of band-averaged data, fluctuated randomly within 6% in UHF and L-band and within 12% in S-band. Judging by the standard deviation of the signal in the off-pulse windows, in all three bands such amount of fluctuation can be attributed to the influence of the background noise. It is worth noting that the "abnormal" mode, observed by Backer & Sallmen (1997) could, in principle, be caused by instrumental error. The average profile of M28A exhibits very high levels of linear polarization with the position angle changing significantly between profile components (Fig. 1(e−f)). If the signal in one of the linear polarizations was for some reason not recorded, then the observed shape of the average profile could be dramatically distorted. We simulated a series of such "abnormal" average profiles by trying different orientations of the Q/U basis on the sky, with the U component of the Stokes vector being subsequently set to zero. For some of the orientations, the resulting profile resembled the "abnormal mode" described in Backer & Sallmen (1997), with intensity of P2 being about three times smaller than the peak intensity of P1.

The logarithmic scale of the ordinate axis in Fig. 1(a) allows very faint profile components to be distinguished (see also the linear-scale zoom-in on Fig. 1(g)). Interestingly, the average profile occupies almost all ($\gtrsim 85\%$) of the spin period, with the only apparent noise window falling at phases 0.882−1.000 (hereafter defined as the "off-pulse window"). Even between P1 and P2 there is radio emission at 0.1 mJy level (with a significance of 5σ, where $\sigma = 0.02$ mJy is the standard deviation of the data within the off-pulse window).

Overall, the shape of the total intensity profile agrees well with profiles at similar frequencies presented by J13 and Yan et al. (2011b). Similar to J13, we record a small dip at the peak of component P1. In the work of Yan et al. (2011b), this dip seems to be washed-out by the intra-channel dispersive smearing in their data. According to Table 1 from their work, the dispersive smearing corresponded to about 0.016 spin periods, commensurate with the width of the dip in our data.

Fig. 1(b−c) show M28A's X-ray and γ-ray average profiles together with their models. Both the profiles and the model parameters were taken from J13. We aligned the high-energy profiles with our radio data by noting that the radio profile from J13, produced with the same ephemeris as that used for the high-energy light curves, has the peak of P1 at phase 0, whereas in our
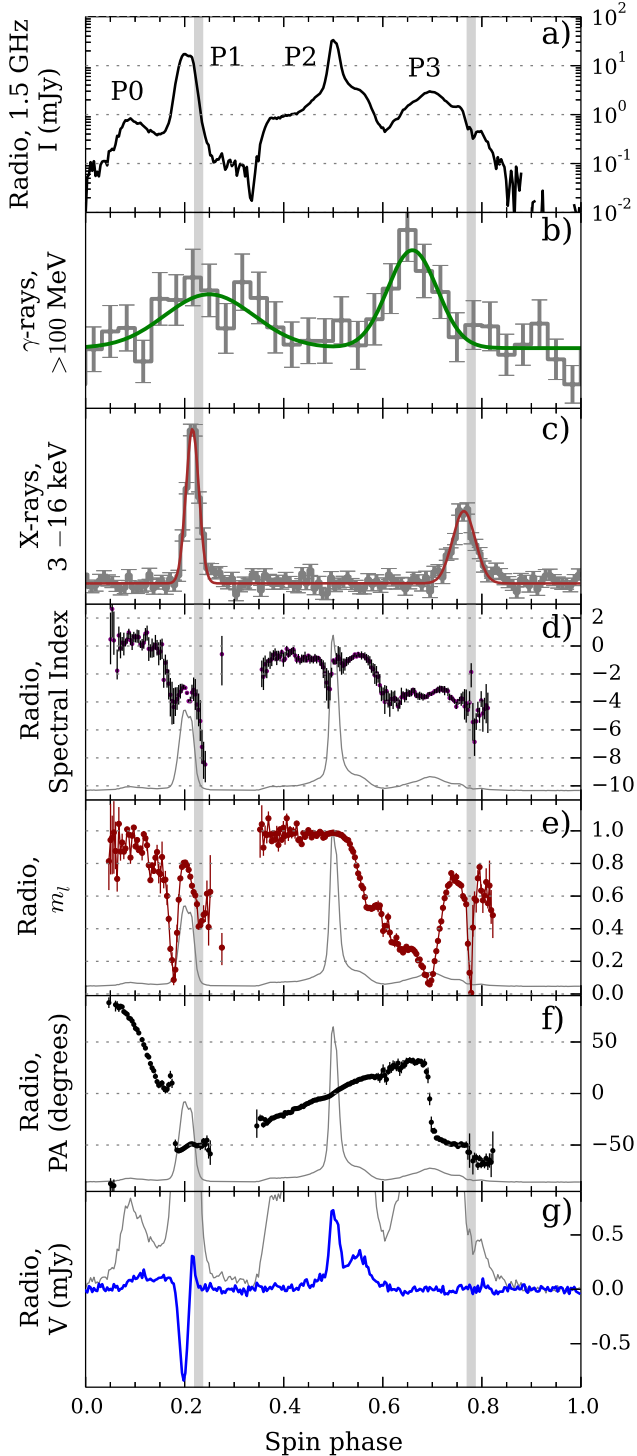
Figure 1. Phase-resolved properties of M28A's average profile in L-band (1100−1900 MHz) together with the X-ray and γ-ray profiles from J13 (see text for details on the alignment). *(a)* total intensity of the radio emission I on a log scale; *(b,c)* γ-ray and X-ray profiles together with their respective models (J13); *(d,e,f)* phase-resolved spectral indices, fractional linear polarization and relative position angle of the radio emission; *(g)* circular polarization V with the total intensity profile *(grey)* overplotted on the same scale. In subplots *(d-f)*, the total intensity profile from subplot *(a)* was overplotted for reference with the intensity on the linear scale. The grey-shaded areas mark the regions with GP emission.

Table 2
Spectral indices of emission, averaged within the individual components in the 1100−2400 MHz frequency range. The data from L- and S-band were combined. P0 stands for the faint precursor to component P1.

	Phase window	Spectral index
P0	$0.05 - 0.15$	0.38 ± 0.1
P1	$0.15 - 0.25$	-3.50 ± 0.04
P2	$0.35 - 0.60$	-1.40 ± 0.03
P3	$0.60 - 0.85$	-3.61 ± 0.05

phase convention the peak of P1 falls at phase 0.2. The grey-shaded areas indicate regions of GP emission (Section 4.1) in all subplots of Fig. 1.

The rest of the subplots in Fig. 1 feature the phase-resolved measurements of spectral indices and polarization of M28A's emission. We show the results obtained from L-band only. The average profile in S-band yields similar results, but with worse S/N, and the emission from the UHF band is scattered by an amount approximately ten times larger than the $10.24\,\mu$s time resolution, making phase-resolved fits unreasonable.

Phase-resolved spectral indices of M28A's radio emission in L-band are shown on Fig. 1(d), with the average profile overplotted for reference[11]. The indices were measured by fitting a power-law function $I = I_0(\nu/\nu_0)^s$ (where $\nu_0 = 1500\,$MHz and ν goes from 1100 to 1900 MHz) to the total intensity in each phase bin[12]. As is expected for a pulsar with strong profile evolution, $s(\phi)$ show considerable amount of variation across the on-pulse windows. It must be noted, though, that the apparent behavior of the phase-resolved spectral indices may be influenced by the frequency-dependent variation of components' position and width. For the former, neither visual inspection nor the analysis in PDR14 show any significant changes in the position of the main components within each separate band. However, profile components become narrower with increasing frequency, which is causing the steepening of the spectral indices at the component edges. Also, the behavior of $s(\phi)$ in any regions with large $|dI/d\phi|$ is sensitive to the DM used for folding, which is reflected by the larger errorbars in these regions (Section 2.2). Scattering, with its steep dependence on observing frequency, can also contribute to the steepening of the measured spectral index at the trailing edge of a sharp profile component.

Except for the steepening in the regions with large $|dI/d\phi|$, the values of $s(\phi)$ stay roughly similar within four broad phase windows corresponding to P0, P1, P2 and P3. In order to compare the spectral indices more readily to the information available for other MSPs (Section 5), we obtained the spectral indices of emission, averaged within each of the four regions. For this fit, we

---

[11] The average profile is identical to the one on Fig. 1(a), but with intensity on a linear scale.

[12] Another approach to measuring spectral indices is given in PDR14, where they approximate the profile with the sum of several Gaussian components and fit a power-law frequency dependence to the position, width and the height of each component.
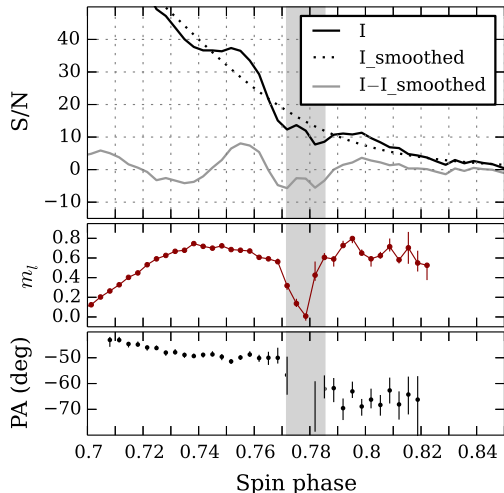
Figure 2. *From top to bottom*: zoom-in on the total intensity (in units of S/N), fractional linear polarization, and PA on a trailing edge of component P3. The 'W'-shaped feature at the phase 0.777 resembles a double notch, which is an absorption feature observed previously in a few other pulsars that can potentially provide clues to the microphysics of pulsar emission (Dyks & Rudak 2012). The grey-shaded area marks the region where GPs occur.

combined the data from L- and S-bands, but omitted the UHF session, since the scattering time in that band corresponded to a significant (30%) fraction of the width of components P0 or P1. The results are presented in Table 2.

The average profile of M28A is very strongly linearly polarized, and has only a small degree of circular polarization. In this work we discuss only relative position angles of the linearly polarized emission, setting PA($\phi = 0.5$) to 0. Generally, both the amount of linear polarization and the relative PA showed the same phase-resolved behavior in all three bands. However, the S/N of the signal was lower in S-band and any rapid variation of $m_l(\phi)$ and PA(ϕ) were washed out by scattering in the UHF band. In L-band, the shape of the PA curve is similar to the one from Yan et al. (2011b)[13].

Both P0 and most of the component P2 are almost completely linearly polarized, with opposite signs of PA gradient. Components P1 and P3 are less polarized, with $m_l < 0.8$. There are two large jumps in PA: one by ΔPA $= 50°$ right before the start of P1 and another one at the peak of P3 (ΔPA $\approx 90°$). Both jumps are accompanied by drops in m_l. Interestingly, there is also a drop in m_l in both regions of GP emission: at the trailing edge of P1 m_l falls to 0.4 and at the trailing edge of P3 m_l is almost 0.

The exceptionally high S/N of the average profile in L-band allowed us to detect an interesting feature on the trailing edge of component P3 (Fig. 2). As was pointed out by J. Dyks (private communication), a 'W'-shaped dip in the total intensity profile around phase 0.777 resembles the so-called "double notches", observed previously in the average profiles of normal pulsars B0950+08, B1919+10 and the MSP J0437−4715 (Dyks & Rudak 2012, and references therein). Double notches were proposed to be a result of a double eclipse in the pulsar

_____

[13] Note that Yan et al. (2011b) report absolute position angles and their measurements cover less of the on-pulse window.

magnetosphere (Wright 2004) or a representation of the shape of a microscopic beam of emitted coherent radiation (Dyks et al. 2007; Dyks & Rudak 2012).

We compared the properties of M28A's dips with the properties of double notches in the literature. The depth of M28A's feature (the drop of the total intensity flux I in the minima with respect to the flux right outside the feature) is about 30%, assuming that the phase window $0.882 < \phi < 1.000$ does not contain pulsar emission. This agrees with the depth of double notches (20%−50%, Dyks & Rudak 2012). For the previously observed double notches, their local minima approached each other with increasing frequency as $\nu^{-0.5}$. Unfortunately, we were unable to explore the frequency-dependent dip separation for M28A, since the combination of a steep spectrum of the underlying component and the increasing role of scattering at lower frequencies make M28A's feature visible only in a limited frequency range (between 1100 and 1600 MHz). Interestingly, unlike observed double notches in other pulsars (Dyks et al. 2007), the double feature in M28A coincides with changes in polarization behavior: a drop in m_l and the small, 15° jump in PA. It is unclear whether these changes are connected to the dips or to the region of GP generation, which is partially overlapping with the feature.

Alternatively, the bump around phase 0.777 can be interpreted as being due to the extra flux brought by GPs. The GPs detected in L-band at the trailing edge of P3 contribute only 0.006 mJy to the average pulse flux density in the corresponding phase window (an additional S/N of 0.3 in Fig. 2). Although this value is much smaller than the height of the bump, the actual GP contribution is unknown, since we have no information about the energy distribution of GPs below our detection threshold.

The question of whether this feature in M28A's profile is a double notch still remains open. In any case, the properties of the feature are worth exploring and may provide some clues to conditions in M28A's magnetosphere.

4. GIANT PULSES

The nature of GPs is far from being understood and even the precise definition of GP has not been established yet. In this work, we will define GPs as individual pulses which have power-law energy distribution and either narrow widths ($< 10\,\mu$s) or substructure on nanosecond timescales (see discussion in Knight 2006).

Our time resolution was not sufficient to resolve the temporal structure of the recorded pulses. However, all of the pulses detected in our study were found within the same phase regions where GPs were previously found by Romani & Johnston (2001) and K06a. Also, the energy distribution of the detected pulses in our study was the same as that of the μs-long GPs from the fine time resolution study of K06a. Therefore, we conclude that our pulses are GPs in the sense of the aforementioned definition.

In total, we have collected 476 GPs with S/N>7 on the band-averaged, calibrated total intensity data. The number of observed pulses per band and window of occurrence is given in Table 3. Our sample is almost 20 times larger than that in Knight et al. (2006a) and the pulses in our work were recorded within 10 times larger frequency band. Thus, we can make better measurements of the

Table 3
Number of GPs detected in each band in each of the two phase windows falling at the trailing edges of components P1 and P3.

Band	P1	P3
UHF	27	12
L	273	81
S	64	19

pulse energy distribution and for the first time probe the instantaneous broadband spectra of a large number of individual GPs.

4.1. *Phase of occurrence*

The leading edge of GPs detected in L- and S-band fell inside a phase window with a width of 0.013 (corresponding to four phase bins or $41\,\mu$s) starting at phases 0.221 and 0.772. In the UHF band, the GP window was also four bins wide, but four times longer due to having four times lower time resolution. K06a, based on a much smaller number of GPs detected with better time resolution, reported the width of the P1 GP window to be 0.006 spin periods, or $18\,\mu$s. This indicates that our width of GP window may be overestimated, most probably because of the coarse $t_{\rm res}$ and, to some extent, the imperfect DM corrections (see Section 2.2).

Both GP windows are within the on-pulse phase range of X-ray profile components (Fig. 1(b)). However, for both P1 and P3 GPs we noticed that the peaks of the X-ray components from J13 are 0.013/0.015 spin periods ahead of the centers of GP windows. Although this is in qualitative agreement with the slight misalignment between the peaks of the X-ray profile components and the centers of GP windows presented in Fig. 1 of K06a, the magnitude of the lag must be taken with caution until measured by direct comparison of radio and X-ray data folded with the same ephemeris.

4.2. *Pulse widths*

While searching for GPs, we defined the width of each GP candidate as the width of the boxcar function which led to the largest peak value in the convolved signal (Section 2.1). Thus, our measured width of GPs could assume only integer multiples of the sampling time $t_{\rm res}$. In S-band and some of the sessions in L-band all GPs had widths of 1 or 2 samples ($10-20\,\mu$s), indicating that the pulses were unresolved (2-sample GPs can occur when the pulse falls between the phase bins). This agrees with K06a, who measured the FWHM of GPs to be between $750\,$ns and $6\,\mu$s at $1341\,$MHz. For some of the sessions in L-band, the GPs were wider and had a clear scattering tail. GPs in the UHF band had widths of $1-4$ samples ($41-164\,\mu$s) and strong GPs showed clear signs of scattering.

4.3. *Energy distribution*

The cumulative energy distributions for P1 and P3 GPs are shown in Fig. 3. In order to reduce the influence of refractive scintillation, in each session GP energies were normalized by the energy of the average profile
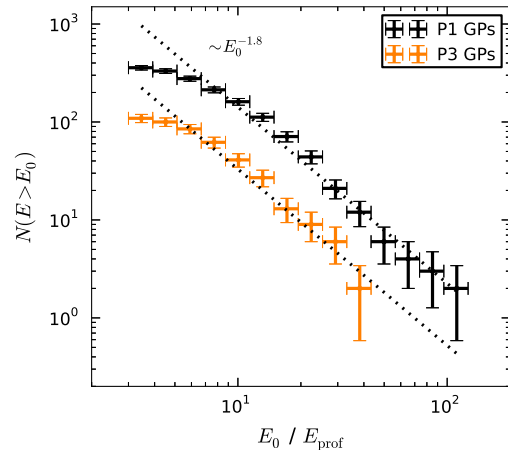

Figure 3. Cumulative energy distributions for GPs coming from the trailing edges of components P1 and P3 in all three observing bands. The errorbars correspond to the $\sqrt{N}$ Poisson uncertainties and do not account for the under-representation of low-energy GPs in our sample. The low-energy end of distribution is affected by a number of selection effects, described in the text.

on that day, $E_{\rm prof}$. Distributions from different bands did not show any substantial difference, so we combined all GPs together. We believe that the flattening of the distribution at the low-energy side is due to the under-representation of the pulses close to the S/N threshold, caused by: a) the width-dependent selection threshold (see Section 2.1); b) the variation of pulsar flux between the sessions due to refractive scintillation (same S/N threshold corresponds to different $E/E_{\rm prof}$); c) slow variation of background noise within each session due to an increased atmospheric path length when the pulsar was approaching the horizon.

Both P1 and P3 GPs have a power-law energy distribution with an index of -1.8 ± 0.3[14], in agreement with -1.6 from K06a. The strongest pulses in all three bands had energies about 100 times larger than the typical energy of the average profile on that session. Since GPs occupy less than 1% of pulsar phase, the mean flux during such pulses exceed the average pulsar flux by $> 10^4$ times.

4.4. *Spectra and polarization*

Despite having observed in a quite narrow band ($64\,$MHz), K06a noticed some prominent frequency variability in the spectra of individual GPs, which led the authors to suggest that GP spectra consist of a series of narrow-band patches. Having observed with a much larger bandwidth, we can clearly see patchy structure in the spectra of individual GPs (Fig. 4). The patches occur more or less uniformly across the observing bands and they cannot be caused by scintillation due to multipath propagation in the ISM – the decorrelation bandwidth is much smaller than the width of any single frequency channel at all our observing frequencies.

After visual examination, we failed to notice any difference between the spectra of P1 and P3 GPs. However, interestingly, the characteristic size of the frequency structure was noted to vary from pulse to pulse. We

---

[14] The uncertainty was obtained by varying the lowest energy threshold used in the power-law fit.
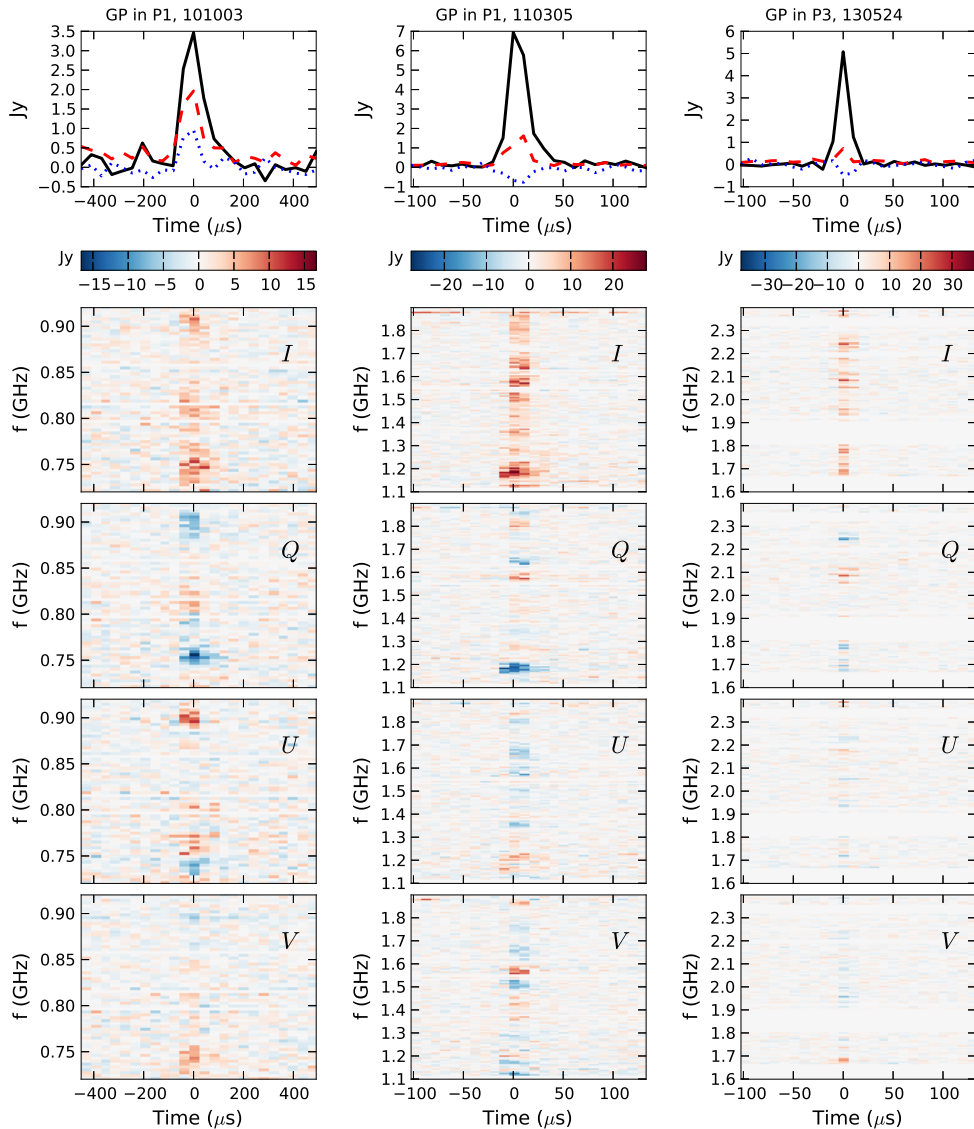
Figure 4. Examples of GPs from the three observed bands in four Stokes components. The phase window of arrival (trailing edge of component P1 or P3) is labeled on top together with the observing date in *yymmdd* format. The top row features band-integrated emission, with total intensity I (*solid black line*), linear polarisation $\sqrt{Q^2 + U^2}$ (*red dashed line*) and circular polarization V (*dotted blue line*). The rest of each column shows the spectra of GPs from the top row in each of the four Stokes components. The GPs are mostly unresolved in time and have exponential scattering tails at lower frequencies (at the bottom of the UHF and L-band observation). Note that both the time and frequency resolutions of the UHF data are four times lower than in L- and S-bands. The decorrelation bandwidth of scintillation due to multipath propagation in the ISM is much smaller than the width of the frequency channels. Thus, the observed frequency structure is an intrinsic property of M28A's GPs. The polarization was corrected for Faraday rotation from the interstellar medium and Earth's ionosphere (see Section 2.3). Within the GPs, the position angle of linear polarization and the sign of circular polarization varies from patch to patch. Therefore, band-integrated GPs have a smaller degree of linear and/or circular polarization.

explored the size of the frequency structure by constructing auto-correlation functions (ACFs) for the one-dimensional spectra of bright pulses with S/N > 20. Pulses were averaged in the phases of their respective detection windows. For L- and S-bands, the characteristic size of the frequency structure was about $10-100\,\mathrm{MHz}$, varying from pulse to pulse. Two illustrative examples of GPs with 100 MHz and 10 MHz structure are shown in Fig. 5. These pulses, both P1 GPs, were recorded during the same L-band observation 20 minutes apart from each other (note that such a dramatic change in the frequency scale of the GP polarization features within a single observing session also implies that these features

are unlikely due to calibration errors). For GPs in the UHF band the width of the patch did not exceed 50 MHz, although only 11 sufficiently bright GPs were available for the analysis and a larger number of pulses is needed to confirm any statistical trend.

Emission within a single patch tends to be strongly polarized, with the position angle of linear polarization and the hand of the circular polarization varying randomly from patch to patch, and sometimes within a single patch (Figs. 4, 5). Fig. 6 shows the fractional linear and circular polarizations for both band-integrated GPs and the individual 1.56 MHz frequency channels. Here we selected only those band-integrated GPs, or GPs from individual
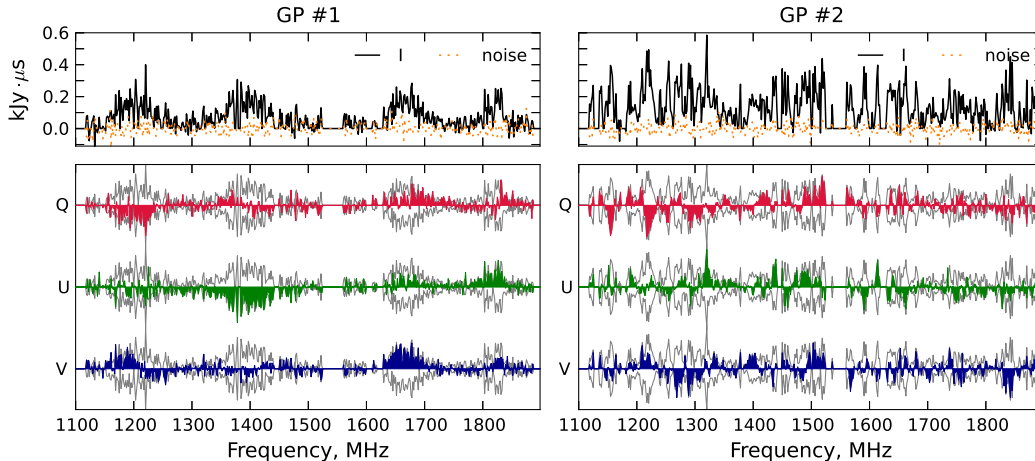
Figure 5. Spectra of two P1 GPs recorded 20 minutes apart from each other. *Top:* the total intensity of GP $I(\nu)$ (black line) and the level of noise outside the pulse (orange dots). The signal in some of the channels was set to zero because of RFI. *Bottom:* the three other components of the Stokes vector for the same pulses. $I(\nu)$ and $-I(\nu)$ are plotted in grey together with each polarized component for reference. The GP on the left shows visible ~ 100 MHz clumps with polarization being constant or changing slowly within each clump. The GP on the right has a more complex frequency structure, presumably consisting of ≈ 10 MHz clumps with similar polarization behavior.
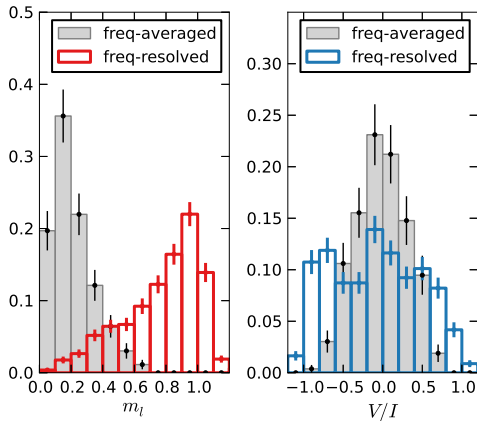

Figure 6. Fractional polarization of GPs: linear (left) and circular (right). Filled bars show the band-integrated fractional polarization for all GPs with S/N > 15. Hollow bars show the polarization per 1.56 MHz frequency channel for all channels where the S/N of the total intensity signal was > 15. Histograms are normalized by the sum of bar heights and Poisson errors are shown on top of each bar. Apparent fractional polarization with magnitude above 100% is due to the influence of noise (see text for details). Individual GP patches tend to be more polarized, but the PA varies from patch to patch which causes gradual washing-out of the polarization across the band. Depending on the intrinsic GP width (which is unresolved in our single-pulse data), the presented polarization measurements may be biased by small-number statistics, and thus may not reflect the intrinsic polarization properties of the GP emission mechanism (see text for details).

channels, for which the S/N of the total intensity was larger than 15. The calculated fractional polarization incorporates contributions from the Stokes components of both the pulsar and the noise. The Stokes components of the noise fluctuate independently from each other around a mean value of 0 with an RMS of 1 (in units of S/N). Thus, when the pulsar signal has a high level of polarization, the absolute value of the calculated fractional polarization can occasionally exceed 1 (Fig. 6). Increasing the S/N threshold for total intensity reduced the number of such "over-polarized" data points, as expected. Overall, band-integrated GPs tend to have smaller fractional

polarization, both linear and circular.

It must be noted that the observed degree of polarization of individual GPs (both frequency-resolved and band-integrated) can be affected by small-number statistics. As was demonstrated by van Straten (2009), if the time-bandwidth product of recorded pulses is on the order of unity, then the observed degree of polarization does not reflect the intrinsic degree of polarization of the source. Although each time sample in our single-pulse data was obtained by averaging 16 (for each frequency channel) or 8192 (for band-averaged data) raw voltage samples (see Section 2), the effective number of independent samples can be small if the average is dominated by one or a few bright nano-pulses (note that scatter-broadening produces correlated samples and thus does not add to the number of degrees of freedom in the average).

The overall average GPs, obtained by summing all GPs in their respective bands, appear to be unpolarized. For L-band, which had the largest number of GP detections, such an average (band-integrated) GP had less than 2% of both fractional linear and circular polarizations.

4.5. *Comparison to GPs from other pulsars*

Combining the measurements from this work and from K06a, we can conclude that the observed properties of M28A's GPs, such as their short (ns−μs) duration, high brightness temperature (up to 5×10^{37} K), narrow (18 μs) window of occurrence, power-law energy distribution with the index of about −1.8, and the probability of detecting GPs with $E > 20E_{\rm prof}$ in a given period, $P(E > 20E_{\rm prof}) \approx 3 \times 10^{-5}$ make the GPs from M28A rather typical members of the GP population[15] (Knight et al. 2005; Knight 2006; Knight et al. 2006b).

---

[15] The currently known GP emitters (in the sense of our GP definition given at the beginning of the section) are M28A, the Crab pulsar, B1937+21, B1820-30A, B1957+20 and J0218+4232. Strong pulses from another young pulsar, B0540-69 are similar to the Crab GPs, but their intrinsic width have not yet been identified because of the strong scattering in the ISM (Johnston & Romani 2003).

It is interesting to compare M28A's GP spectra together with their polarization properties to the spectral structure and polarization of GPs from the most studied GP pulsars, B1937+21 and the Crab pulsar.

GPs from PSR B1937+21 have a characteristic width of tens of nanoseconds (Soglasnov et al. 2004) and thus are usually unresolved. Popov & Stappers (2003) observed PSR B1937+21 at 1430 MHz and 2230 MHz simultaneously, with an instrumental fractional bandwidth ($\Delta\nu_{inst}/\nu$) of 0.01 and 0.02. During the three hours of observing time, spread among multiple sessions, 25 GPs were recorded, with none of them occurring at both frequencies simultaneously. This led the authors to conclude that GPs from PSR B1937+21 have frequency structure with a scale of $\Delta\nu_{GP}/\nu \approx 0.5$. In addition, some GPs in their study showed variability on a smaller frequency scale $\Delta\nu_{GP}/\nu \approx 0.007$, which could not be explained by diffractive scintillation. Numerous observations with narrow fractional bandwidths ($\Delta\nu_{inst}/\nu$ ranging from 0.001 to 0.03) revealed that most of the GPs from PSR B1937+21 show strong circular and a considerable amount of linear polarization, both varying randomly from pulse to pulse (Cognard et al. 1996; Popov et al. 2004; Kondratiev et al. 2007; Zhuravlev et al. 2011). Soglasnov (2007) presented an unusual example of a resolved GP, composed of two nano-pulses with different hands of circular polarization. However, all aforementioned works present polarization measurements for individual data samples (unresolved GPs or unresolved components), thus the reported degree of polarization must be biased by small-number statistics (van Straten 2009).

On larger frequency scales, GPs from the Crab pulsar exhibit similar frequency modulation with $\Delta\nu_{GP}/\nu$ on the order of 0.5 (Popov et al. 2008, 2009). On smaller frequency scales, the situation is more complex since it is known that at frequencies above 4 GHz, Crab GPs from the main pulse component (MGPs) and the GPs from the interpulse component (IGPs) have very different spectral and polarization properties (Hankins et al. 2003; Hankins & Eilek 2007).

MGPs consist of a series of nanosecond-long unresolved pulses (called nanoshots), which often merge together into so-called microbursts (see, for example, Fig. 1 in Hankins et al. 2003). Nanoshots are quite narrow-band, with $\Delta\nu_{GP}/\nu \approx 0.03$ (Hankins & Eilek 2007). The studies of polarized emission conducted by Hankins et al. (2003) and Jessner et al. (2010) showed that individual unresolved nanoshots are strongly circularly or linearly polarized, with the hand of V changing randomly from shot to shot. This leads to weak polarization of MGPs if the radio emission is averaged within a pulse (Hankins & Eilek 2007). Both below and above 4 GHz, microbursts from the Crab's MGPs are known to have broadband ($\Delta\nu_{GP}/\nu$ between, approximately, 0.3 and 1, Crossley et al. 2010) spectra, with a scale of fine structure $\Delta\nu_{GP}/\nu$ ranging from 0.003 to 0.01 (Popov et al. 2008, 2009; Jessner et al. 2010).

The GPs from the interpulse do not have nanosecond-scale structure above 4 GHz and their spectra are dramatically different from those of MGPs. The IGP spectra consist of bands, proportionally spaced in frequency with $\Delta\nu/\nu = 0.06$ (Hankins & Eilek 2007). The width of the band is $10-20\%$ of the spacing between the

bands and sometimes bands can shift upwards in frequency within a single GP (see, for example, Fig. 7 in Hankins & Eilek 2007). Jessner et al. (2010) studied the polarization smoothed within 80 ns windows (32 samples) for IGPs recorded within $\Delta\nu_{inst}/\nu \approx 0.06$ and report high degree of linear polarization (up to 100%) and a flat PA curve. Below 4 GHz there are hints that IGPs have properties similar to those of MGPs (Crossley et al. 2010; Zhuravlev et al. 2013) but more detailed studies are needed.

Due to our coarse time resolution, we can not compare directly the temporal structure of M28A's GPs to that of the Crab's MGPs/IGPs. We do not notice any well-defined, persistent periodicity in the separation between the patches in GP spectra, although we must notice that our 100 MHz modulation has $\Delta\nu/\nu$ of about $0.04-0.09$, similar to the $\Delta\nu/\nu = 0.06$ spacing between the IGP bands. Some of our less modulated spectra could be caused by bands drifting up in frequency and smearing the periodic structure. Above 4 GHz, IGPs of the Crab pulsar have widths of about 3 µs (Jessner et al. 2010). If M28A's GPs have similar widths, the pulses are resolved and each frequency channel in our data contains several independent samples. In this case, the observed degree of polarization may serve as a more or less adequate estimate of the intrinsic GP polarization. However, our polarization statistics are hard to compare to that of Jessner et al. (2010) because of the differences in the observing setups. We found no published polarization properties of separate frequency bands of Crab IGPs, and thus we do not know if the hand of the circular or the PA of linear polarization can vary between the bands of the same GP.

We find the idea that M28A's GPs consist of individual nanoshots somewhat more compelling. K06a showed an example of two strong pulses from M28A observed simultaneously at 2.7 and 3.5 GHz. One pulse consisted of a single peak with FWHM of 20 ns, another GP showed multiple unresolved (< 7.8 ns) spikes, some of which merged together, forming a burst of about 200 ns. Such behavior is similar to the Crab MGPs. For M28A's GP spectra with well-defined patches, the characteristic scale of frequency modulation is close to the spectral width of the Crab's nanoshots, $\Delta\nu_{GP}/\nu \approx 0.03$. The Crab's individual nanoshots are strongly and randomly polarized and we observe the same for individual patches within a single M28A's GP (Fig 5, left). Thus, M28A's GPs, with their well-defined patches, could consist of several separate, unresolved, narrow-band nanoshots[16], with a seemingly large apparent degree of polarization. The finer frequency modulation in some of M28A's GP spectra (Fig 5, right) has the same order of magnitude as the modulation found in the microbursts of Crab GPs. Being composed of a larger number of overlapping nanoshots would also explain why such GPs have more rapid variation of polarization with frequency.

Combining the known spectral and temporal properties of GPs from the PSR B1937+21, M28A and the Crab

---

[16] The aforementioned broadband ($\Delta\nu_{GP}/\nu \approx 0.3$), 20-ns wide GP from K06a does not contradict this conclusion, since K06a derive their value of DM for that session by aligning the times of arrival of the low- and high-frequency parts for the two GPs recorded. Therefore, it is possible that their 20-ns pulse consisted of two separate narrow-band nanoshots.

pulsar, it is tempting to draw a general portrait of a giant pulse. Such a portrait generalizes the information already available, but these generalizations must be further tested with a series of dedicated studies. One may speculate that a "typical giant pulse" consists of random number of individual, narrow-band nanoshots. Nanoshots appear to be strongly and randomly polarized, although the intrinsic degree of polarization should be constrained by the future studies with much better time resolution. The number of nanoshots per pulse appears to be bound by some upper limit, and this limit seems to be correlated with the pulsar spin period. GPs from PSR B1937+21, the pulsar with the smallest spin period ($P = 1.6$ ms) among all known GP emitters, consist of one or, very rarely, two nanoshots and that is why Popov & Stappers (2003) failed to detect B1937+21's GPs simultaneously at two widely separated frequencies. GPs from M28A ($P = 3.05$ ms) have up to several nanoshots, which we have observed as patches in GP spectra. Finally, the Crab pulsar's MGPs ($P = 33$ ms) are usually made of much larger number of nanoshots which merge together and create continuous spectra. The Crab's IGPs, with their lack of temporal structure and banded spectra, clearly do not fit this picture and present a separate puzzle.

5. M28A IN THE CONTEXT OF OTHER γ-RAY MSPS

Here we will review the properties of M28A's multiwavelength emission in the context of tendencies and trends observed among the MSPs from the second Fermi catalog. Although M28A, due to its large $\dot{E}$, always was a promising candidate to search for γ-ray pulsations, the relatively large distance and unfortunate location (both in the Galactic plane and in the heart of a globular cluster) made the detection complicated: it took about 190 weeks of Fermi data to detect 5.4σ pulsations (J13). M28A's light curves have not been modeled yet and J13 note that it might be a complex case, possibly going beyond the standard models. Thus, a comparison to other, better studied γ-ray MSPs is important.

According to Johnson et al. (2014, hereafter J14), the MSPs from the second Fermi catalog fall into three categories and each category can be more or less well modeled using the simple assumptions about the location of radio/γ-ray emission regions. For the pulsars with γ-ray peaks trailing the radio peaks (so-called Class I, after Venter et al. 2012) high-energy emission is believed to come from the broad range of altitudes close to the light cylinder, originating inside the narrow vacuum gap at the border of the surface of last-closed field lines (Cheng et al. 1986; Muslimov & Harding 2003; Dyks & Rudak 2003). Radio emission of Class I pulsars is thought to come from the open field region above the polar cap and is modeled with the core and/or hollow cone components. Both the core and the cone are uniformly illuminated in magnetic azimuth (meaning, not patchy) and have the size determined by the statistical radius-to-frequency mapping prescriptions (Story et al. 2007). For the Class II pulsars, the γ-ray peaks are nearly (within about 0.1 spin periods) aligned with the radio peaks, and, unlike Class I, Class II radio emission is assumed to originate in the regions significantly extended in altitude and co-located with the γ-ray emission regions (Abdo et al. 2010; Venter et al. 2012; Guillemot et al.

2012)[17]. Pulsars with γ-ray peaks leading the radio peaks are labeled as Class III. In this case, the radio emission has the same origin as for the Class I pulsars, but high-energy emission comes from high altitudes above the polar cap volume (Harding et al. 2005)[18].

Figure 7 shows M28A on the standard $P - \dot{P}$ diagram for the MSPs from the second Fermi catalog. It is very important to remember that the observed spin-down rate of MSPs can be greatly influenced by Doppler effects originating from the pulsar's proper motion (Shklovskii 1970) and the acceleration in the local gravitational field. The additional apparent spin-down due to the Shklovskii effect ($\delta\dot{P}_{\rm Sh}$) depends on the pulsar period, the distance to the source, and its proper motion. $\delta\dot{P}_{\rm Sh}$ is always > 0 and can be responsible for a large fraction of the observed $\dot{P}$, whereas $\delta\dot{P}$ due to acceleration can have either sign, but is usually much smaller than the Shklovskii effect (see Table 6 in Abdo et al. 2013). The uncertainties in estimating Doppler corrections are included in the errorbars[19] on $\dot{P}$ in Fig. 7. For the pulsars with unknown proper motion, the observed $\dot{P}$ can be viewed as an upper limit on the intrinsic spin-down rate. Such pulsars are marked with unfilled markers. The classes were assigned to pulsars prior to modeling and were mostly based on the lags between their radio and γ-ray peaks. In some cases, the classification differs between J14 and Ng et al. (2014). In Fig. 7 such pulsars are featured with a question mark inside their markers.

Long before the γ-ray detection of M28A, Backer & Sallmen (1997), based on the alignment between radio and X-ray profile, put forward the idea that M28A's radio components P1 and P3 may be of caustic origin, whereas P2 comes from above the polar cap. Up to now there have been no attempts to model such "mixed-type" radio profiles (J14), however, previous studies showed that caustic radio emission may have properties somewhat different from the cone/core components and that it seems to be limited to the pulsars occupying a specific region on $P - \dot{P}$ diagram (Espinoza et al. 2013; Ng et al. 2014, but see discussion in J14). Below we review the properties of pulsars with both types of radio emission and compare them to those of M28A.

5.1. *Magnetic field at the light cylinder*

The MSPs with the highest values of $B_{\rm LC}$[20] tend to be Class II pulsars (J14; Espinoza et al. 2013; Ng et al.

[17] Class II pulsars can also be modeled with both γ-ray and radio emission coming from the small range of heights close to the stellar surface inside the narrow gap close to the last open field line (Venter et al. 2012). However, this model results in worse fits to the data, according to J14.

[18] There exist other models for γ-ray emission (Qiao et al. 2004; Du et al. 2010; Pétri 2009), as well as more detailed (patched cone) models of the radio profiles of MSPs (Craig 2014), but we will not focus on them in this work.

[19] While most of the proper motion and distance values were taken from the second Fermi catalog, for PSR J0218+4232 we used the proper motion of 6.53 ± 0.08 mas yr^{-1} measured by Du et al. (2014) and the distance obtained from the parallax measurements in the same work, but corrected for the Lutz-Kelker bias by Verbiest & Lorimer (2014).

[20] The magnetic field at the light cylinder was calculated with a classical dipole formula, by assuming that a pulsar is an orthogonal rotator and loses its rotational energy only via magnetic dipole
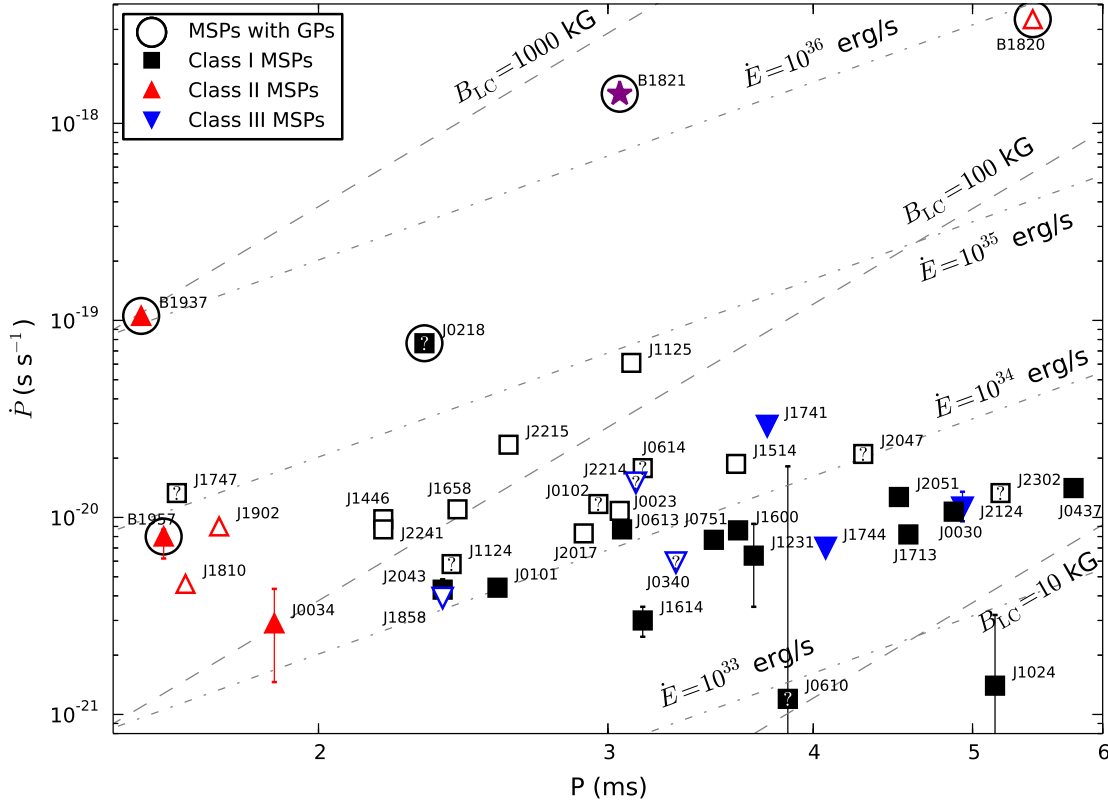
Figure 7. M28A (marked with a purple star) on the $P - \dot{P}$ diagram of the MSPs from the second Fermi catalog. The names of the pulsars are truncated after right ascension and correspond to the full names in Fig. 8. The errorbars reflect the estimated uncertainty in $\dot{P}$ due to the Shklovskii effect and accelerated motion in a gravitational potential. The pulsars without proper motion measurements are shown with unfilled markers. Following the classification in J14, Class I pulsars are shown with black squares, Class II with red upward triangles and Class III with the blue downward triangles. Pulsars which have a different classification in Ng et al. (2014) are featured with a question mark. Pulsars with known GPs are circumscribed with a circle. Dashed lines show constant $B_{\rm LC}$ and the dot-dashed lines mark constant $\dot{E}$.

2014). From Fig. 7, we notice that J0034−0534 has the lowest value of $B_{\rm LC}$ among "clear" Class II MSPs, $B_{\rm LC} \approx 100\,{\rm kG}$. However, some of the pulsars with $B_{\rm LC} < 100\,{\rm kG}$ have one of the radio components roughly (within 0.1 spin periods) coinciding with a γ-ray one, for example (but not limited to) PSRs J0340+4130, J2214+3000 and J2302+4442 (J14). Thus, it is possible that caustic radio emission can originate from pulsars with $B_{\rm LC} < 100\,{\rm kG}$. Confirmation might be obtained by direct modeling and/or by studying the profile evolution and polarizational properties of the radio emission from these pulsars.

Thirteen MSPs from the second Fermi catalog lie above $B_{\rm LC} \approx 100\,{\rm kG}$ line. Out of these pulsars, six had been identified as Class II by J14 and Ng et al. (2014). Out of these six, three do not have proper motion measurements – J1902−5105, J1810+1744 and B1820−30A, although for the latter there is indirect evidence that the observed $\dot{P}$ is an adequate estimate of the intrinsic pulsar spin-down. PSR B1820−30A is a luminous γ-ray source and any reasonable assumptions about the γ-ray efficiency

radiation. The influence of plasma currents and non-orthogonal magnetospheric geometry may alter the values of $B_{\rm LC}$ to some poorly known extent (Guillemot & Tauris 2014).

leads to the conclusion that most of the observed $\dot{P}$ is intrinsic (Freire et al. 2011). The average radio profile of one of these pulsars, PSR B1957+20, has an additional component which does not match any of the γ-ray peaks and was not modeled by J14.

Two pulsars with Shklovskii-corrected $B_{\rm LC} \approx 300\,{\rm kG}$ had been modeled as Class I in J14: J0218+4232 and J1747−4036. PSR J0218+4232 has very broad radio profile, with radio emission coming from virtually all spin phases, and has a large unpulsed fraction (Navarro et al. 1995). The brighter broad radio component falls at the minimum of the γ-ray profile (which consist of one very broad component), but there is a second, more faint radio peak with a seemingly steeper spectral index (Stairs et al. 1999). This component is not modeled by J14 and it is aligned with the γ-ray emission. Ng et al. (2014) classifies PSR J0218+4232 as Class II. PSR J1747−4036 is a newly-discovered (Kerr et al. 2012) pulsar that has two components in its radio profile, one of which is aligned with the weak γ-ray peak and the other one is about 0.4 spin periods behind. Ng et al. (2014) classifies this pulsar as Class II/I, whereas J14 classifies it as Class I, although they do not model the second radio peak. According to J14, this pulsar has polarization lev-

els which are not suitable for a Class II pulsar, although we will argue below that not all Class II MSPs have zero linear polarization.

The last five pulsars above the 100 kG line are all clear Class I pulsars, having $B_{LC} < 150$ kG and unknown proper motions.

To summarize, none of the well-established $B_{LC} > 100$ kG MSPs from the second Fermi catalog have a radio profile consisting only of components which have doubtless polar cap (Classes I or III) origin. Such high-B_{LC} pulsars have either only radio components which are aligned with the γ-ray profile or the "mixed-type" radio profile, with some of radio components being aligned and some being not (e.g. PSRs B1957+20, J1747−4036 and perhaps J0218+4232). M28A has a very large value of $B_{LC} = 720$ kG and in its radio profile two of the three radio peaks roughly coincide with the γ-ray peaks, similarly to PSR B1957+20. Thus it is not unreasonable to suppose that these two matching peaks (components P1 and P3) can be of caustic origin.

It is worth noting that for young pulsars from the second Fermi catalog[21], three out of four sources with the highest values of B_{LC} all have 100 kG $< B_{LC} < 150$ kG and their radio profiles are clearly misaligned with the γ-rays. The only known young pulsar with aligned profiles is the Crab pulsar, and it has the largest B_{LC} in the second Fermi catalog, 980 kG.

5.2. *The spectral index of radio emission*

According to Espinoza et al. (2013), Class II pulsars tend to have steeper spectral indices than the bulk of the γ-ray MSPs (or radio MSPs in general). We compiled a database of spectral indices for the MSPs from the second Fermi catalog and plot them in Fig. 8. The pulsars are arranged by decreasing B_{LC}. No spectral information is available for many of them, signifying a good opportunity for future studies. Some of the spectral indices were measured in different frequency bands, and thus the scatter of points for the sources with multiple measurements may reflect an intrinsic departure from a single power-law in the very broad frequency range. However, some of the scatter may reflect unaccounted systematic errors (for example, if available spectra consisted of only a few flux measurements, with some of the measured fluxes affected by scintillation), and so these index values should be taken with caution, especially those with only one measurement.

Generally, pulsars with larger values of B_{LC}, or which are Class II, have steeper spectral indices than the average value for MSPs, $s = -1.8$ (Kramer et al. 1998), whereas Class I and III have shallower indices, although the latter is not true in all cases, e.g. for PSR J0030+0451.

M28A has a quite steep average spectrum, $s = -2.36$ (PDR14), in line with the tendency for the Class II pulsars. Interestingly, components P1 and P3 have much steeper frequency dependence than the component P2 (Table 2), supporting the idea of different magnetospheric origin. It is worth noticing that the same behavior is exhibited by B1957+20, whose shallower component (Fruchter et al. 1990) is misaligned with the γ-rays.

[21] Young pulsars have much larger values of $\dot{P}$ and thus do not suffer from the Shklovskii effect.
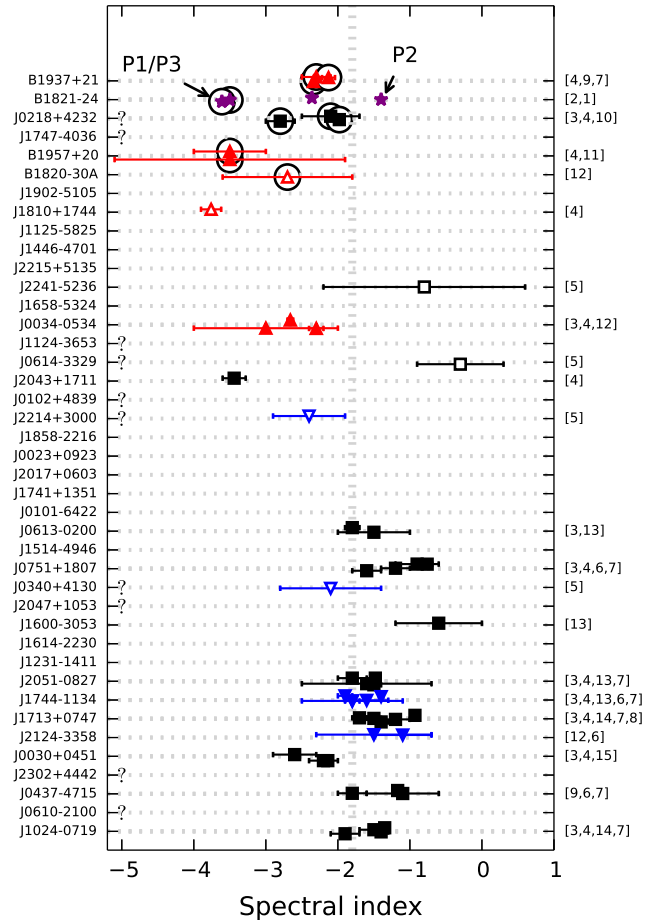

Figure 8. All available spectral indices for the radio emission of MSPs in the second Fermi catalog. Pulsars are sorted by descending values of B_{LC}. The markers follow the same scheme as in Fig. 7. A small random vertical jitter was added to the markers to facilitate the visual examination of the data. A vertical line marks both the mean and the median values of the distribution of MSP spectral indices from Kramer et al. (1998). For M28A, both the spectral index of phase-averaged emission and the indices from individual components are shown. Note that component P2, the one misaligned with the γ-ray components has a shallower spectrum, which is in line with Class I/III pulsars, whereas components P1/P3 have more steep spectra and are roughly aligned with the γ-ray emission. References: [1] this work; [2] PDR14; [3] Kuzmin & Losovsky (2001); [4] Hassall et al in prep; [5] Espinoza et al. (2013); [6] Kramer et al. (1998); [7] Kramer et al. (1999); [8] Kijak et al. (1998); [9] Yan et al. (2011b); [10] Navarro et al. (1995); [11] Fruchter et al. (1990); [12] Toscano et al. (1998); [13] Ord et al. (2004); [14] Xilouris et al. (1998); [15] Lommen et al. (2000).

Finally, the Crab pulsar has the spectral index of -3.1 ± 0.2, unusually steep for a young pulsar (Lorimer et al. 1995), but close to those of the Class II MSPs.

5.3. *Polarization*

As was noticed by Espinoza et al. (2013), pulsars with aligned γ-ray and radio profiles tend to have a very small amount of linear polarization, which is quite unusual for MSPs. Among six Class II MSP PSRs from J14, three are linearly depolarized. These pulsars are J0034−0534, B1820−30A and B1957+20 (Stairs et al. 1999; Fruchter et al. 1990). This fact is usually treated as support for the caustic origin of the radio emission, as

the radio emission gets depolarized coming from different heights (Dyks et al. 2004). However, we must note that the sole presence of polarization in the average profile does not preclude a pulsar from being a Class II. According to Dyks et al. (2004), caustic emission does not necessitate complete depolarization, but rather only a decrease in the fractional polarization, as well as rapid swings and jumps in the position angle.

Two of the pulsars with aligned radio/high-energy emission, B1937+21 and the Crab pulsar show substantial levels of fractional linear polarization: about 0.4 for B1937+21 (Kramer et al. 1999) and about 0.2 for the Crab pulsar (Moffett & Hankins 1999). It is puzzling to note that although the positions of the radio peaks for B1937+21 and the Crab pulsar are best reproduced with a caustic radio emission model (Guillemot et al. 2012; Harding et al. 2008), the PA of the radio emission does not exhibit much variation across the profile components (Ord et al. 2004; Słowikowska et al. 2015). Perhaps more complex models of radio emission are needed, for example the ones which include propagation of radio waves through the magnetosphere.

In M28A, the component P2 shows a greater degree of linear polarization, and the sweep in PA is reminiscent of that predicted by rotating vector model (RVM; Radhakrishnan & Cooke 1969). Components P1 and P3 show a much lower amount of fractional polarization (although the level is still somewhat higher than for B1937+21 or the Crab pulsar) and not much PA variation, except for the seemingly orthogonal jump at the peak of P3. Such PA behavior is similar to that observed in the main and interpulse profile components of both the Crab pulsar and B1937+21.

5.4. *X-ray spectrum and light curves*

According to Zavlin (2007), pulsars with large spin-down energies $\dot{E} > 10^{35}$ erg s^{-1} and short periods $P < 3.1$ ms tend to have non-thermal magnetospheric X-ray emission, and their X-ray profiles have a large pulsed fraction and narrow components. Such X-ray emission is attributed to synchrotron and/or inverse Compton processes in the pulsar magnetosphere. The known MSPs with non-thermal X-ray profiles are M28A, B1937+21 and J0218+4232. For M28A, the X-ray components coincide with the trailing edges of radio components P1/P3.

Two other Class II MSPs, B1820−30A and J0034−0534 have unfavorable positions on the sky, with strong X-ray sources nearby (Migliari et al. 2004; Zavlin 2006). PSR B1957+20 is the prototypical black widow system and a large fraction of its X-rays comes from an intrabinary shock between the pulsar wind and that of the companion star (Huang & Becker 2007). Recently, Guillemot et al. (2012) discovered weak, 4σ X-ray pulsations from this pulsar. The X-ray profile of PSR B1957+20 consists of one broad gaussian-shaped component, which seems to be offset from the γ-ray components, although the authors note that the phase alignment between the γ-ray and X-ray data may not be accurate. PSR J1810+1744 is another example of an MSP in a black-widow system. The X-ray emission from this pulsar shows broad orbital variability, with possible orbit-to-orbit variations (Gentile et al. 2014). So far, there has been no attempt to search for pulsed X-ray

emission from this pulsar. For PSR J1902−5105 only upper limits on its X-ray flux were placed (Takahashi et al. 2012).

To our knowledge, no narrow pulsations of clear non-thermal origin have been detected for any other MSP from the second Fermi catalog (see Table 16 in Abdo et al. 2013). The rest of the sources have blackbody and/or power-law spectra. Broad thermal pulsations have been detected for pulsars J0030+0451, J0751+1807, J2124−3358, J0437−4715 and J1024−0719 (Webb et al. 2004; Zavlin 2006; Bogdanov & Grindlay 2009).

5.5. *Giant pulses*

The idea that GPs are found from pulsars with high values of B_{LC} was proposed a long time ago (Cognard et al. 1996). Excluding M28A and J0218+4232, all known MSPs that emit GPs are Class II γ-ray pulsars (B1937+21, B1957+20 and B1820−30A, three out of five known MSPs with GPs). For PSR B1957+20, the pulsar with a supposedly "mixed-type" radio profile, GPs have been detected only from one of the Class II radio components (Knight et al. 2006b). It must be noted though, that the statistics of GPs from this pulsar are quite limited, as only 4 GPs were ever detected (Knight et al. 2006b).

Knight et al. (2005) failed to find GPs from another Class II pulsar, J0034−0534. However, given the amount of the observing time in Knight et al. (2005), their sensitivity limits, and the estimates on the GP rate from the known GP MSPs (like, for example PSR J0218+4232, Knight et al. 2006b), it is possible that Knight et al. (2005) did not have enough observing time to detect a sufficiently strong GP with peak flux density above their sensitivity threshold. Thus, further searches of GPs from J0034−0534 (as well as from the two other, previously unexplored Class II pulsars, J1902−5105 and J1810+1744) could be promising.

For M28A, the GPs come from the phase regions on the trailing side of components P1/P3, with component P2 being free from any sign of GP emission. If M28As components P1/P3 are of caustic origin, then (omitting the complicated case of PSR J0218+4232 and the distant, young, potential GP pulsar B0540−69 in the Large Magellanic Cloud) we can summarize that all GP pulsars have detected γ-ray components, whose aligned Class II radio components share phase windows with GP emission. Radio emission from such components is believed to originate in narrow gaps and come frome the regions which are both significantly extended in altitude and positioned near the light cylinder. The physical conditions there can be much different from the regions where radio emission is placed traditionally (i.e. at low altitudes and within a small range of heights dictated by radius-to-frequency mapping). This should be taken into account by the theories of GP generation, for example the ones which rely on plasma turbulence (Weatherall 1998) or on the interaction between the low- and high-frequency radio beams (Petrova 2006).

Based on the discussion above, we can conclude that MSPs with large values of $B_{\mathrm{LC}} \gtrsim 100$ kG tend to have properties different from the bulk of MSPs from the second Fermi catalog. One such property is the presence of

caustic radio components. It must be noted that the true character of the "conventional" and the caustic types of radio emission are still to be investigated, since a substantial fraction of MSPs from the second Fermi catalog have been discovered just recently and thus have not been extensively studied in radio yet. For M28A, the components P1/P3 resemble the radio components typical of Class II pulsars (i.e. having a steep spectral index, rough alignment with γ-ray and X-ray profile components and GP phase windows). Component P2 resembles core/cone emission from altitudes above the polar cap (i.e. having a shallow spectral index, no matching high-energy components, and no GPs). The direct modeling of M28A's radio and high-energy profiles promises to be very interesting.

6. SUMMARY

The extensive set of full-Stokes, wideband and multi-frequency observations of M28A with the Green Bank Telescope allowed us to determine a high-fidelity average profile in unprecedented and remarkable detail, as well as to collect the largest known sample of M28A's giant pulses.

Between 1100 and 1900 MHz, we found that M28A's pulsed emission covers more than 85% of the pulsar's rotation. In addition to the three previously described profile components (P1−P3), we distinguish P0 (first spotted by Yan et al. 2011b), a faint component in the phase window right before the component P1. We present measurements of phase-resolved spectral indices and polarization properties throughout almost all of the on-pulse phase window. The phase-resolved spectral indices exhibit prominent variation with spin phase, while at the same time staying roughly similar within four broad phase windows corresponding to components P0−P3.

Components P0 and P2 of M28A's profile are almost completely linearly polarized, whereas the levels of polarization for P1 and P3 are lower. Two of the four recorded drops in the fractional linear polarization coincide with the narrow phase windows of GP generation on the trailing edges of components P1 and P3. The average profile in the phase window of GP generation at the trailing edge of component P3 has a small (15°) jump of the position angle of the linearly polarized emission. Interestingly, in the same phase region, we found an absorption feature which resembles a double notch, a feature which may bring some insight into the microphysics of the pulsar radio emission.

We compare the radio and high-energy properties of M28A to those of MSPs from the second Fermi catalog, and argue that M28A's radio emission can be a mix of caustic and polar cap components. The components P1 and P3, characterized by steep spectral indices and rough alignment with both high-energy profile components and GP phase windows, resemble the caustic radio emission observed previously from PSR B1937+21, B1820−30A and a few other pulsars with a high value of the magnetic field at the radius of the light cylinder. On the other hand, component P2 resembles the traditional core/cone emission from altitudes above the polar cap (i.e. with a shallow spectral index, no matching high-energy components, no detected GPs). The origin of the P0 component (showing a positive spectral index between 1100 and 2400 MHz, a high level of linear polarization, a rapid

PA sweep, and no GPs) remains unclear.

Our measured energy distribution and detection rate for M28A's GPs agrees with previous works. We have also investigated the broadband spectra of M28A's GPs. The spectra appear patchy, with the typical size of a patch changing randomly from pulse to pulse within the limits of 10−100 MHz. Individual patches appear to be strongly polarized, with the direction of the linear and the hand of the circular polarization changed randomly from patch to patch (and sometimes within a single patch). However, depending on the intrinsic GP width (unresolved in our single-pulse data), observed degree of polarization may be biased by small-number statistics (van Straten 2009), and thus may not reflect the intrinsic polarization properties of GP emission mechanism. Unlike the main and interpulse GPs from the Crab pulsar, M28A's GPs from the trailing edges of components P1 and P3 seem to have similar properties to one another. Although our time resolution was not sufficient to resolve the fine temporal structure of individual pulses, we argue that M28A's GPs resemble the GPs from the main pulse of the Crab pulsar, which consist of a series of narrow-band nanoshots.

REFERENCES

Abdo, A. A., Ackermann, M., Ajello, M., Allafort, A., Baldini, L., Ballet, J., Barbiellini, G., et al. 2010, ApJ, 712, 957
Abdo, A. A., Ajello, M., Allafort, A., Baldini, L., Ballet, J., Barbiellini, G., Baring, M. G., et al. 2013, ApJS, 208, 17
Backer, D. C., & Sallmen, S. T. 1997, The Astronomical Journal, 114, 1539
Bilous, A. V., McLaughlin, M. A., Kondratiev, V. I., & Ransom, S. M. 2012, ApJ, 749, 24
Bogdanov, S., & Grindlay, J. E. 2009, ApJ, 703, 1557
Bogdanov, S., van den Berg, M., Servillat, M., Heinke, C. O., Grindlay, J. E., Stairs, I. H., Ransom, S. M., et al. 2011, ApJ, 730, 81
Cheng, K. S., Ho, C., & Ruderman, M. 1986, ApJ, 300, 522
Cognard, I., & Backer, D. C. 2004, ApJ, 612, L125
Cognard, I., Bourgois, G., Lestrade, J.-F., Biraud, F., Aubry, D., Darchy, B., & Drouhin, J.-P. 1996, A&A, 311, 179
Craig, H. A. 2014, ApJ, 790, 102
Crossley, J. H., Eilek, J. A., Hankins, T. H., & Kern, J. S. 2010, ApJ, 722, 1908
Du, Y., Yang, J., Campbell, R. M., Janssen, G., Stappers, B., & Chen, D. 2014, ApJ, 782, L38
Du, Y. J., Qiao, G. J., Han, J. L., Lee, K. J., & Xu, R. X. 2010, MNRAS, 406, 2671
DuPlain, R., Ransom, S., Demorest, P., Brandt, P., Ford, J., & Shelton, A. L. 2008, in Society of Photo-Optical Instrum. Engineers (SPIE) Conference Series, Vol. 7019, 1
Dyks, J., Harding, A. K., & Rudak, B. 2004, ApJ, 606, 1125
Dyks, J., & Rudak, B. 2003, ApJ, 598, 1201
—. 2012, MNRAS, 420, 3403
Dyks, J., Rudak, B., & Rankin, J. M. 2007, A&A, 465, 981

Espinoza, C. M., Guillemot, L., Çelik, Ö., Weltevrede, P., Stappers, B. W., Smith, D. A., Kerr, M., et al. 2013, MNRAS, 430, 571

Foster, R. S., Backer, D. C., Taylor, J. H., & Goss, W. M. 1988, ApJ, 326, L13

Foster, III, R. S. 1990, PhD thesis, California Univ., Berkeley.

Freire, P. C. C., Abdo, A. A., Ajello, M., Allafort, A., Ballet, J., Barbiellini, G., Bastieri, D., et al. 2011, Science, 334, 1107

Fruchter, A. S., Berman, G., Bower, G., Convery, M., Goss, W. M., Hankins, T. H., Klein, J. R., et al. 1990, ApJ, 351, 642

Gentile, P. A., Roberts, M. S. E., McLaughlin, M. A., Camilo, F., Hessels, J. W. T., Kerr, M., Ransom, S. M., et al. 2014, ApJ, 783, 69

Guillemot, L., Johnson, T. J., Venter, C., Kerr, M., Pancrazi, B., Livingstone, M., Janssen, G. H., et al. 2012, ApJ, 744, 33

Guillemot, L., & Tauris, T. M. 2014, MNRAS, 439, 2033

Hankins, T. H., & Eilek, J. A. 2007, ApJ, 670, 693

Hankins, T. H., Kern, J. S., Weatherall, J. C., & Eilek, J. A. 2003, Nature, 422, 141

Harding, A. K., Stern, J. V., Dyks, J., & Frackowiak, M. 2008, ApJ, 680, 1378

Harding, A. K., Usov, V. V., & Muslimov, A. G. 2005, ApJ, 622, 531

Hotan, A. W., van Straten, W., & Manchester, R. N. 2004, Proc. Astron. Soc., 21, 302

Huang, H. H., & Becker, W. 2007, A&A, 463, L5

Jessner, A., Popov, M. V., Kondratiev, V. I., Kovalev, Y. Y., Graham, D., Zensus, A., Soglasnov, V. A., et al. 2010, A&A, 524, A60

Johnson, T. J., Guillemot, L., Kerr, M., Cognard, I., Ray, P. S., Wolff, M. T., Bégin, S., et al. 2013, ApJ, 778, 106

Johnson, T. J., Venter, C., Harding, A. K., Guillemot, L., Smith, D. A., Kramer, M., Çelik, Ö., et al. 2014, ApJS, 213, 6

Johnston, S., & Romani, R. W. 2003, ApJ, 590, L95

Kerr, M., Camilo, F., Johnson, T. J., Ferrara, E. C., Guillemot, L., Harding, A. K., Hessels, J., et al. 2012, ApJ, 748, L2

Kijak, J., Kramer, M., Wielebinski, R., & Jessner, A. 1998, A&AS, 127, 153

Knight, H. S. 2006, Chinese Journal of Astronomy and Astrophysics Supplement, 6, 41

Knight, H. S., Bailes, M., Manchester, R. N., & Ord, S. M. 2005, ApJ, 625, 951

—. 2006a, ApJ, 653, 580

Knight, H. S., Bailes, M., Manchester, R. N., Ord, S. M., & Jacoby, B. A. 2006b, ApJ, 640, 941

Kondratiev, V. I., Popov, M. V., Soglasnov, V. A., Kovalev, Y. Y., Bartel, N., & Ghigo, F. 2007, in WE-Heraeus Seminar on Neutron Stars and Pulsars 40 years after the Discovery, ed. W. Becker & H. H. Huang, 76

Kramer, M., Lange, C., Lorimer, D. R., Backer, D. C., Xilouris, K. M., Jessner, A., & Wielebinski, R. 1999, ApJ, 526, 957

Kramer, M., Xilouris, K. M., Lorimer, D. R., Doroshenko, O., Jessner, A., Wielebinski, R., Wolszczan, A., & Camilo, F. 1998, ApJ, 501, 270

Kuzmin, A. D., & Losovsky, B. Y. 2001, A&A, 368, 230

Lommen, A. N., Zepka, A., Backer, D. C., McLaughlin, M., Cordes, J. M., Arzoumanian, Z., & Xilouris, K. 2000, ApJ, 545, 1007

Lorimer, D. R., Yates, J. A., Lyne, A. G., & Gould, D. M. 1995, MNRAS, 273, 411

Lyne, A. G., Brinklow, A., Middleditch, J., Kulkarni, S. R., & Backer, D. C. 1987, Nature, 328, 399

Migliari, S., Fender, R. P., Rupen, M., Wachter, S., Jonker, P. G., Homan, J., & van der Klis, M. 2004, MNRAS, 351, 186

Moffett, D. A., & Hankins, T. H. 1999, ApJ, 522, 1046

Muslimov, A. G., & Harding, A. K. 2003, ApJ, 588, 430

Navarro, J., de Bruyn, A. G., Frail, D. A., Kulkarni, S. R., & Lyne, A. G. 1995, ApJ, 455, L55

Ng, C.-Y., Takata, J., Leung, G. C. K., Cheng, K. S., & Philippopoulos, P. 2014, ApJ, 787, 167

Ord, S. M., van Straten, W., Hotan, A. W., & Bailes, M. 2004, MNRAS, 352, 804

Pennucci, T. T., Demorest, P. B., & Ransom, S. M. 2014, ApJ, 790, 93

Pétri, J. 2009, A&A, 503, 13

Petrova, S. A. 2006, Chinese Journal of Astronomy and Astrophysics Supplement, 6, 113

Popov, M., Soglasnov, V., Kondratiev, V., Bilous, A., Moshkina, O., Oreshko, V., Ilyasov, Y., et al. 2009, PASJ, 61, 1197

Popov, M. V., Soglasnov, V. A., Kondrat'ev, V. I., Bilous, A. V., Sazankov, S. V., Smirnov, A. I., Kanevskiĭ, B. Z., et al. 2008, Astronomy Reports, 52, 900

Popov, M. V., Soglasnov, V. A., Kondrat'ev, V. I., & Kostyuk, S. V. 2004, Astronomy Letters, 30, 95

Popov, M. V., & Stappers, B. 2003, Astronomy Reports, 47, 660

Qiao, G. J., Lee, K. J., Wang, H. G., Xu, R. X., & Han, J. L. 2004, ApJ, 606, L49

Radhakrishnan, V., & Cooke, D. J. 1969, Astrophys. Lett., 3, 225

Ransom, S. M. 2001, PhD thesis, Harvard University

Rickett, B. 1996, in Astronomical Society of the Pacific Conference Series, Vol. 105, IAU Colloq. 160: Pulsars: Problems and Progress, ed. S. Johnston, M. A. Walker, & M. Bailes, 439

Romani, R. W., & Johnston, S. 2001, The Astrophysical Journal, 557, L93

Saito, Y., Kawai, N., Kamae, T., Shibata, S., Dotani, T., & Kulkarni, S. R. 1997, ApJ, 477, L37

Shklovskii, I. S. 1970, Soviet Ast., 13, 562

Słowikowska, A., Stappers, B. W., Harding, A. K., O'Dell, S. L., Elsner, R. F., van der Horst, A. J., & Weisskopf, M. C. 2015, ApJ, 799, 70

Soglasnov, V. 2007, in WE-Heraeus Seminar on Neutron Stars and Pulsars 40 years after the Discovery, ed. W. Becker & H. H. Huang, 68

Soglasnov, V. A., Popov, M. V., Bartel, N., Cannon, W., Novikov, A. Y., Kondratiev, V. I., & Altunin, V. I. 2004, ApJ, 616, 439

Sotomayor-Beltran, C., Sobey, C., Hessels, J. W. T., de Bruyn, G., Noutsos, A., Alexov, A., Anderson, J., et al. 2013, A&A, 552, A58

Stairs, I. H., Thorsett, S. E., & Camilo, F. 1999, ApJS, 123, 627

Story, S. A., Gonthier, P. L., & Harding, A. K. 2007, ApJ, 671, 713

Takahashi, Y., Kataoka, J., Nakamori, T., Maeda, K., Makiya, R., Totani, T., Cheung, C. C., et al. 2012, ApJ, 747, 64

Toscano, M., Bailes, M., Manchester, R. N., & Sandhu, J. S. 1998, ApJ, 506, 863

van Straten, W. 2004, ApJS, 152, 129

—. 2009, ApJ, 694, 1413

van Straten, W., Demorest, P., & Oslowski, S. 2012, Astronomical Research and Technology, 9, 237

van Straten, W., Manchester, R. N., Johnston, S., & Reynolds, J. E. 2010, PASA, 27, 104

Venter, C., Johnson, T. J., & Harding, A. K. 2012, ApJ, 744, 34

Verbiest, J., Bailes, M., Coles, W., Hobbs, G., van Straten, W., Champion, D., Jenet, F., et al. 2009, Monthly Notices of the Royal Astronomical Society, 400, 951

Verbiest, J. P. W., & Lorimer, D. R. 2014, MNRAS, 444, 1859

Weatherall, J. C. 1998, ApJ, 506, 341

Webb, N. A., Olive, J.-F., Barret, D., Kramer, M., Cognard, I., & Löhmer, O. 2004, A&A, 419, 269

Wright, G. A. E. 2004, MNRAS, 351, 813

Wu, J. H. K., Hui, C. Y., Wu, E. M. H., Kong, A. K. H., Huang, R. H. H., Tam, P. H. T., Takata, J., & Cheng, K. S. 2013, ApJ, 765, L47

Xilouris, K. M., Kramer, M., Jessner, A., von Hoensbroech, A., Lorimer, D. R., Wielebinski, R., Wolszczan, A., & Camilo, F. 1998, ApJ, 501, 286

Yan, W. M., Manchester, R. N., Hobbs, G., van Straten, W., Reynolds, J. E., Wang, N., et al. 2011a, 335, 485

Yan, W. M., Manchester, R. N., van Straten, W., Reynolds, J. E., Hobbs, G., Wang, N., et al. 2011b, MNRAS, 414, 2087

Zavlin, V. E. 2006, ApJ, 638, 951

—. 2007, Ap&SS, 308, 297

Zhuravlev, V. I., Popov, M. V., Kondrat'ev, V. I., Kovalev, Y. Y., Ghigo, F., & Soglasnov, V. A. 2011, Astronomy Reports, 55, 724

Zhuravlev, V. I., Popov, M. V., Soglasnov, V. A., Kondrat'ev, V. I., Kovalev, Y. Y., Bartel, N., & Ghigo, F. 2013, MNRAS, 430, 2815